Progress In Electromagnetics Research, Vol. 147, 203–226, 2014

Performance Enhancement of Microwave Sub-Wavelength Imaging and Lens-Type DOA Estimation Systems by Using Signal Processing Techniques

Xiang Gu[1, 2], Raj Mittra[1, *], Chiara Pelletti[1], Sidharath Jain[3], and Yunhua Zhang[2]

(*Invited Paper*)

Abstract—In this work, we show how we can improve the image resolution capabilities of a Phase Conjugating (PC) lens as well as the angular resolution of Luneburg lens antennas by employing signal processing techniques such as the Correlation Method (CM), the Minimum Residual Power Search Method (MRPSM), the sparse reconstruction method, and the Singular-Value-Decomposition (SVD)-based basis matrix method. In the first part, we apply these techniques for sub-wavelength imaging in the microwave regime by combining them with the well-known phase conjugation principle. We begin by considering a one-dimensional microwave sub-wavelength imaging problem handled by using three signal processing methods, and then we move on to two- or three-dimensional problems by using the SVD-based basis matrix method. Numerical simulation results show that we can enhance the resolution significantly by using these methods, even if the measurement plane is not located in the very near-field region of the source. We describe these proposed algorithms in detail and study their abilities to resolve at the sub-wavelength level. Next, we investigate the sparse reconstruction method for a normal Luneburg lens antenna and the Correlation Method and the SVD-based basis matrix method for a flat-base Luneburg lens antenna to estimate the Direction-of-Arrival (DOA). Numerical simulation results show that the signal processing techniques are capable of enhancing the angular resolution of the Luneburg lens antenna enabling the lens to locate multiple targets with different scattering cross-sections and achieving higher angular resolution.

1. INTRODUCTION

The problem of achieving high resolution focusing by using a "superlenses"or a "perfect lens" [1, 2] has recently attracted considerable attention of researchers since they have the potential to overcome the diffraction limit and achieve superior resolution in microwave imaging and in angle estimation type of problems.

In microwave imaging, the topics of Phase Conjugation (PC), as well as Time Reversal Mirrors (TRM) have been thoroughly investigated and a great deal of research has been conducted [3, 4]. Microwave imaging with a resolution at the sub-wavelength level is attractive in many applications, which include: high-directivity arrays used in modern self-tracking wireless communication systems [5]; electromagnetic sounding of 3D structures of an inhomogeneous dielectric half-space for nanophysics, biological and medical diagnostics [6]; and short-range Ultra-wide Band (UWB) radar imaging [7], to name a few. Many approaches have been proposed for microwave sub-wavelength imaging, including nonlinear metamaterial elements [8], periodic layered metal-dielectric structures [9], metallic screens comprised of closely spaced and unequal slits [10], Fresnel zone-plates [11], etc. Several devices based

Accepted 14 January 2015, Accepted 2 February 2015, Scheduled 8 February 2015

* Corresponding author: Raj Mittra (Mittra@engr.psu.edu).

[1] The Electromagnetic Communication Laboratory, Department of Electrical Engineering, The Pennsylvania State University, University Park, PA 16802, USA. [2] The Key Laboratory of Microwave Remote Sensing, Center for Space Science and Applied Research, Chinese Academy of Sciences, Beijing 100190, China. [3] Microsoft, One Microsoft Way, Redmond, WA 98052, USA.

on PC lens have been reported, e.g., a phase conjugating lens consisting of a double-sided assembly of straight wire elements [12], metallic strip gratings which perform evanescent-to-propagating wave conversion [13], sub-wavelength array of planar monopoles [14] and split-ring resonators loaded with varactor diodes [15], etc.

However, the applications of the current techniques still pose huge challenges. For instance, to realizing a "superlens" by using artificial materials or matematerials not only poses many practical difficulties, but complex is costly as well. Moreover, a common feature of these existing imaging techniques is that they must rely on the availability of near-field information, which is not too convenient in practice. Recently, signal processing techniques have been proposed into lens imaging to achieve improved resolution [16, 17]. In [18–22], signal processing techniques for sub-wavelength imaging in the microwave regime by combining them with the PC lens, namely the Correlation Method (CM) [18], the Minimum Residual Power Search Method (MRPSM) [19, 20], the sparse reconstruction method [18], and the Singular-Value-Decomposition (SVD)-based basis matrix method [21, 22]. We demonstrate in this work that these techniques can achieve sub-wavelength resolution even when the measurement plane is not located in the near-field region of the source. The proposed techniques are detailed below and their abilities to resolve at the sub-wavelength level are examined.

In the Direction-of-Arrival (DOA) estimation problem, wide-angle scanning and high angular resolution are often desired in many applications, e.g., wireless communication, air navigation, automotive radar, etc. [23, 24], and mechanically steerable antennas are traditionally used for such applications. However, such antennas are usually operated by a mechanical rotation type of device which cannot meet the requirements of rapid beam-scanning and flexible control. It is well-known that phased arrays are more sophisticated and can serve multiple functions for different applications. However, they can be bulky, expensive to fabricate and often require signal processing hardware. The Luneburg lens [25], which has the capability of all-angles can regardless of the frequency of operation, as well as excellent focusing characteristics, is an attractive candidate for many applications such as multi-beam antennas, multi-frequency scanning, and spatial scanning [26, 27]. Many researchers have focused on the problem of manufacturing and realization of the Luneburg lens, including the design and implementation of two-dimensional (2D) or three-dimensional (3D) Luneburg lens antennas. Unfortunately, its applications in the area of DOA estimation are rarely mentioned.

In [28], Xin et al. reported an approach for detecting a single target by using five conformal detectors located on the curved surface of a single Luneburg lens antenna to receive the signal from -20° to 20° The operating frequency is 5.6 GHz, and the initial direction finding results from using a correlation algorithm showing that the estimated error is smaller than 2° within the angular range of incident angles from -15° to 15°. However, the range of incident angles is still limited, and the number of detectors (5) is not adequate to achieve the desired level of accuracy. Recently, we have proposed a novel flat-base Luneburg lens antenna, and have investigated its scan performance and compared it with conventional lenses [29]. Based on the previous studies, we propose the use of a Luneburg lens antenna for DOA estimation by using signal processing techniques, i.e., the sparse reconstruction method, the CM [30], the SVD based basis matrix method. Numerical results show that, we can not only achieve both wide-angle scanning and high-angular resolution by utilizing signal processing techniques, we can also operate over a broad frequency range and for different polarizations.

2. MICROWAVE SUB-WAVELENGTH IMAGING WITH A PHASE CONJUGATION LENS

2.1. One-dimensional Microwave Sub-wavelength Imaging

2.1.1. Principle of Phase Conjugation Lens

A representative scheme of microwave sub-wavelength imaging via the use of Phase Conjugating (PC) lens is shown in Fig. 1. The test objects are y-oriented Perfect Electric Conductor (PEC) strips illuminated by a plane wave, that are located in the x-y plane (source plane) at $z = 0$. The scattered field distribution is first measured over a grid set up on the measurement plane at $z = d$. Next, the measured data is phase conjugated and propagated to the image plane at $z = 2d$ to obtain an image of the original object in the image plane.

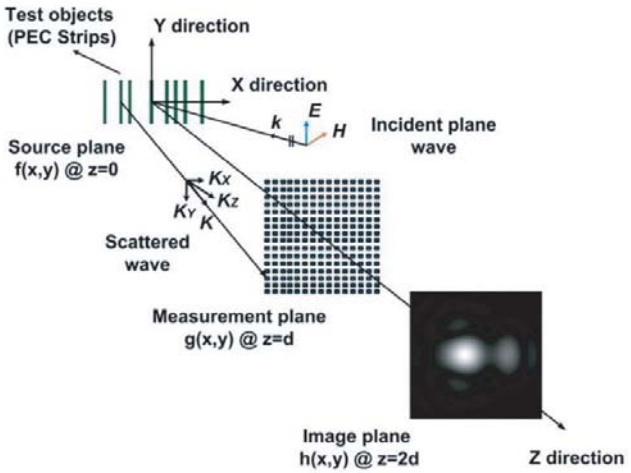

Figure 1. Scheme for microwave sub-wavelength imaging via PC.

The distributions in the object, measurement and image planes can be related by using a transform method. The Fourier transform of the spatial field distribution over the x-y plane located at $z = 0$ can be expressed as:

$$F(k_x, k_y, z = 0) = \int_{-\infty}^{\infty} \int_{-\infty}^{\infty} f(x, y, z = 0)\, e^{jk_x x} e^{jk_y y} dx dy \tag{1}$$

where k_x and k_y denote the spectral variables; $f(x, y, z = 0)$ and $F(k_x, k_y, z = 0)$ represent the spatial and spectral distributions at the source plane, respectively.

Next, the spectrum $G(k_x, k_y, z = d)$ at the measurement plane can be derived as follows by propagating $F(k_x, k_y, z = 0)$ at a distance d along the z-direction:

$$G(k_x, k_y, z = d) = F(k_x, k_y, z = 0) e^{-jk_z d} \tag{2}$$

The wavenumber k_z in the z-direction is related to k_x, k_y and $k(k = 2\pi/\lambda)$ as follows:

$$k_z = \begin{cases} \sqrt{k^2 - (k_x^2 + k_y^2)} & \text{when} \quad k_x^2 + k_y^2 < k^2 \quad \text{(3a)} \\ -j\sqrt{(k_x^2 + k_y^2) - k^2} & \text{when} \quad k_x^2 + k_y^2 \geq k^2 \quad \text{(3b)} \end{cases}$$

The form of k_z, as expressed by (3a), corresponds to the propagating waves (visible part of the spectrum), while (3b) defines the evanescent waves (invisible range of the spectrum).

The next step involves phase conjugating and propagating the spectrum $G(k_x, k_y, z = d)$ to the image plane to derive $H(k_x, k_y, z = 2d)$. This is accomplished by using the expression shown below:

$$H(k_x, k_y, z = 2d) = G^*(-k_x, -k_y, z = d)\, e^{-jk_z d} = F^*(-k_x, -k_y, z = 0) \tag{4}$$

which relates the spectrum at the image plane to that at the source plane.

After having performed the operations of Fourier transform, phase conjugation, and propagation to the image plane, we find that the spectrum at the image plane is a "flipped" (with respect to the spectral variables k_x and k_y) and conjugated version of the original spectrum at the source plane. By applying the well-known properties of Fourier transforms, the relationship between the spatial field distribution at the source and image planes can be expressed as follows:

$$h(x, y, z = 2d) = f^*(x, y, z = 0) \tag{5}$$

It is evident that the spatial field distribution at the image plane is the conjugate of the original spatial field distribution at the source plane.

In general, if the phase conjugating lens is positioned in the far-field region of the sources, its resolution is always diffraction-limited, because the evanescent component of the spectrum carrying sub-wavelength information cannot reach the phase-conjugating surface.

2.1.2. Correlation Method

Next, we consider the problem of generating an image for an arbitrary combination of PEC strips, whose number is unknown as yet, and which have sub-wavelength separation distances. We begin by describing the Correlation Method (CM), which is widely used in signal processing.

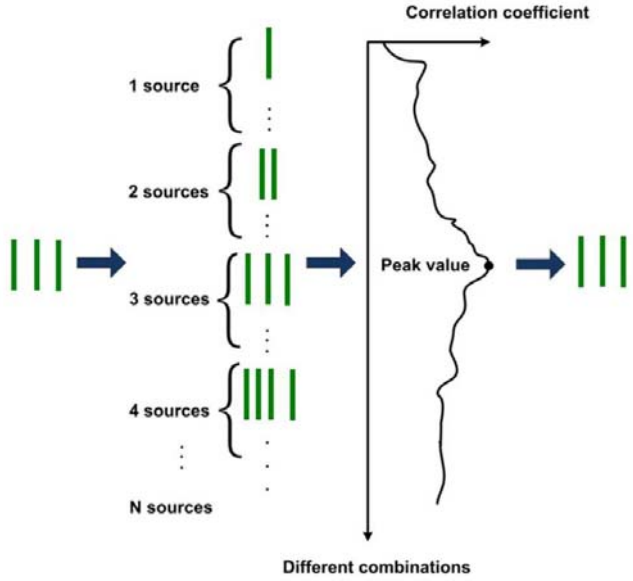

Figure 2. Representative scheme of CM.

As shown in Fig. 2, we assume that an arbitrary number of sources are present at the source plane, ranging from a single source, to a maximum number N. For each combination, we calculate the radiated fields at the measurement plane and then correlate them with the measured data. The peak value of the correlation coefficients is used to determine the correct position of the original sources at the source plane.

The CM is based on correlating the field distribution generated by each of the assumed combinations of sources with the original one. Without loss of generality, we assume that we are dealing with the E_y-component of the electric field. The correlation coefficient is defined as:

$$Corr.coef(n) = \frac{1}{(M_i M_j - 1)\sigma_M \sigma_A} \sum_{i=1}^{M_i} \sum_{j=1}^{M_j} \left[(E^M(x_i, y_j) - \mu_M)(E_n^A(x_i, y_j) - \mu_A)^* \right] \tag{6}$$

where μ_M and μ_A represent the mean value of the field distribution of the assumed combinations of sources (subscript 'A') and the measured field ('M'), while σ_M and σ_A are their standard deviations; respectively. M_i and M_j are the numbers of samples along x and y gathered at the measurement plane. Here the correlation coefficients are complex; hence, we compare their magnitudes.

Specifically, all of the combinations are generated in a search area first identified using the image obtained by applying the phase conjugation algorithm. The search is not carried out at locations where the values of the normalized image fall below a certain threshold level, say 0.5.

The CM can achieve a very high resolution if one can accurately locate the maximum correlation coefficient. However, the CM approach has some limitations of its own. First, the maximum correlation coefficient used to determine the correct source combination is only slightly larger than the one which is the next highest, especially when the sources are close to each other or the Signal-to-Noise Ratio (SNR) is not high. Secondly, during the process of searching for the sources, the number of combinations to be considered can become very large and the computational burden can increase dramatically. For example, when the sources are randomly distributed in 10 positions, the number of combinations is 2^{10}; however, it rises to 2^{20} when the source distribution involves 20 unknowns.

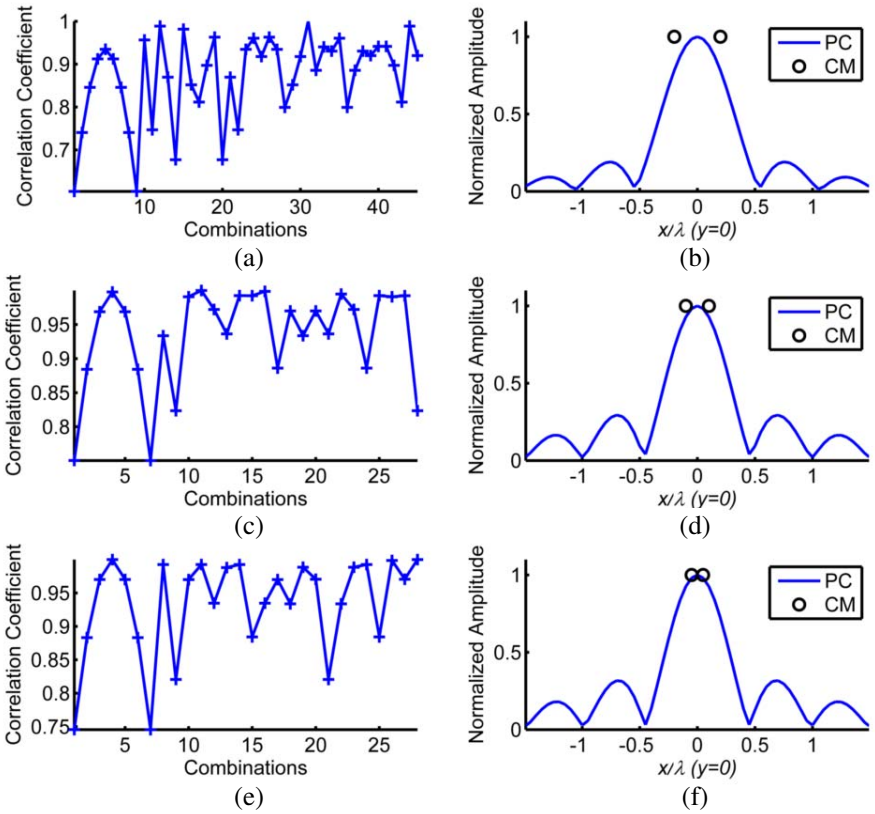

Figure 3. Correlation coefficients (left column) as a function of the considered combination of sources when the separation distance is (a) $2\lambda/5$, (c) $\lambda/5$ and (e) $\lambda/10$; and normalized spatial images (right column) obtained by PC(solid line) and CM (circle marker) when the separation distance is (b) $2\lambda/5$, (d) $\lambda/5$ and (f) $\lambda/10$.

In the discussion presented above, we have assumed that the magnitudes of the sources are all equal. If we wish to include sources with different strengths, we must consider an additional degree of freedom, which will further increase the number of required operations, and will negatively impact upon the computational efficiency of the CM.

For the CM, we set the operating frequency to be 10 GHz, the spatial sampling rate at the measurement plane to be $\lambda/20$ and the number of samples as 801 and the aperture size is 40λ. We assume that the distance d between the source and measurement planes as λ. We consider two sources centered at the origin along the x-direction, and their separation distance is $2\lambda/5$, $\lambda/5$ and $\lambda/10$; respectively.

Figure 3 shows variations of the correlation coefficients (left column) as a function of the considered combinations of sources when the separation distance is (a) $2\lambda/5$, (c) $\lambda/5$ and (e) $\lambda/10$. The spatial images (right column) are derived by using the phase conjugation and the CM when the separation distances are: (b) $2\lambda/5$; (d) $\lambda/5$; and (f) $\lambda/10$. In the CM, we search for the maximum correlation coefficient, which corresponds to the correct combination of the sources. The present example shows that for a moderate number of sources, the CM performs well and is able to achieve sub-wavelength resolution, even with separation distances as small as $\lambda/10$.

2.1.3. Minimum Residual Power Search Method

To circumvent some of the issues encountered in Subsubsection 2.1.2 with the CM when the number of sources is not small, we apply the Minimum Residual Power Search Method (MRPSM), which systematically adjusts the local distribution of the sources by using an iterative minimum residual

power search algorithm to obtain both the numbers and the positions of the sources.

The step-by-step procedure for this method is as follows:

1) Generate the image result from the measurement data by using the PC method.
2) Extract the $y = 0$ cut from the image result and normalize the curve.
3) Determine the image region, N_{IR}, by using the criterion where this region only covers the locations where the level of the normalized field is higher than a preset threshold δV, e.g., $\delta V = 0.5$.
4) Set the local adjustment region to be N_{LAR}.
5) Find the position of the maximum value of the normalized $y = 0$ cut curve.
6) Adjust the local source distribution in the neighbourhood of this position with the local adjustment region N_{LAR}, and calculate the image field of each source distribution.
7) Search the source distribution which has the minimum power of the residual between the image field generated by the measured data and that calculated by the assumed source distribution, according to the Minimum Residual Power Criterion (MRPC).
8) Repeat until the search is finished and all the combinations of the source distribution within the image region N_{IR} have been considered.
9) Take the distribution which has the minimum power of the residual as the final result.

The MRPC is defined as:

$$\Delta(n) = \min\left\{\sum_{i=1}^{M_i}\sum_{j=1}^{M_j}\left|E^M(x_i, y_j) - E^A(x_i, y_j)\right|^2\right\} \tag{7}$$

where E^M represents the field distribution of the measured field ('M'), and E^A represents the field distribution of the assumed combinations of sources (subscript 'A') at the n-th search step, in which the sources are rearranged only in the local adjustment region. The quantity $\Delta(n)$ represents the minimum power of the residual at the n-th step.

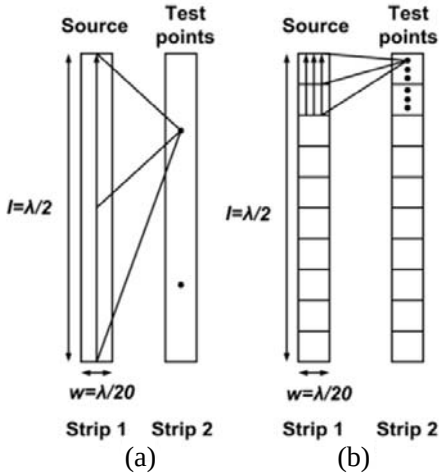

Figure 4. Schematic representations of (a) SMBFs and (b) SRBFs.

In both CM and MRPSM approaches, we need to calculate the field distributions emanating from different combinations of these objects and then correlate or compare them to the measured field. To numerically model the current distribution over the sources, we employ either the Sinusoidal Macro Basis Functions (SMBFs) [31], or the Sinusoidal Rooftop Basis Functions (SRBFs) [32].

As shown in Fig. 4, SMBFs assume that the induced surface current on the PEC strips is sinusoidal over the entire length of the dipole, while when using SRBFs, the current distribution is modelled as

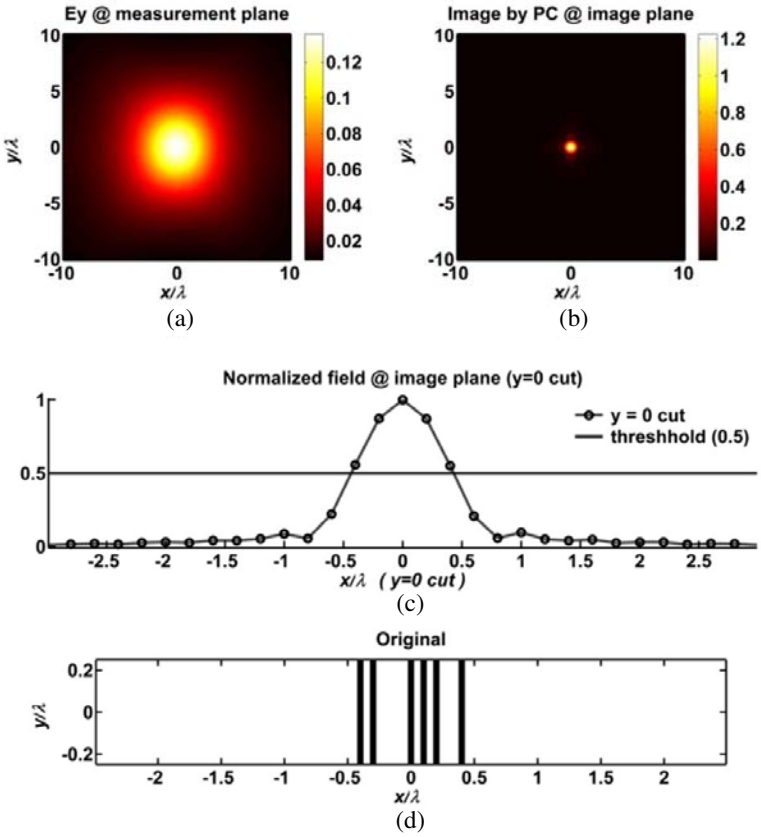

Figure 5. (a) E_y field distribution at the measurement plane; (b) image recovered by PC at the image plane; (c) normalized magnitude of E_y at the image plane ($y = 0$ cut) with a preset threshold, i.e., 0.5; and (d) original source distribution; black strips represent the PEC strips.

a superposition of sinusoidal rooftop type of basis functions. Typically, when using SRBFs, a half-wavelength strip whose length and width are $\lambda/2$ and $\lambda/20$, respectively, is divided into 10 and 3 sections in the x- and y-directions, respectively, and this makes the number of unknowns of the current distribution to be 27 times larger than that when we use the SMBFs method. However, SRBFs yield results with much higher accuracy than do the SMBFs because of the more accurate current distribution model.

Numerical simulations of different distributions of PEC strips have been carried out by using the FEKO 6.2 Suite [33] to generate the "measured" data. Due to physical constraints, the aperture size cannot be chosen as large as desired. In the following examples, we set the operating frequency to be 1 GHz, the distance between the source and measurement planes to be 5λ, and the observation aperture size to be 20λ. The equivalent sources are y-oriented PEC strips, each with length $\lambda/2$ and width $\lambda/20$, respectively. The sampling interval is $\lambda/5$, both in the x- and y-directions, while the corresponding number of samples in the measurement plane is 101.

For the first case, 6 PEC strips are located at the following x positions: $(-4, -3, 0, 1, 2, 4) \times \lambda/10$, as shown in Fig. 5(d), and they are illuminated normally by a TE-polarized plane wave. Fig. 5(a) shows the electric field distribution observed over an aperture size of $20\lambda \times 20\lambda$ at the measurement plane, and it is simulated by using FEKO 6.2 Suite. Fig. 5(b) shows the image generated by utilizing PC only, and it is apparent that this technique alone is unable to resolve the position of the sources,even though the maximum interval between the sources is $3\lambda/10$. Fig. 5(c) shows the $y = 0$ cut of the normalized field distribution at the image plane. We set the threshold δV to be 0.5, and find that the region in the image plane where the values of the normalized field is above $\delta V = 0.5$ ranges from $-2\lambda/5$ to $2\lambda/5$. We set the unit interval to be $\lambda/10$, so this image region contains 9 unknown units, implying that $N_{IR} = 9$.

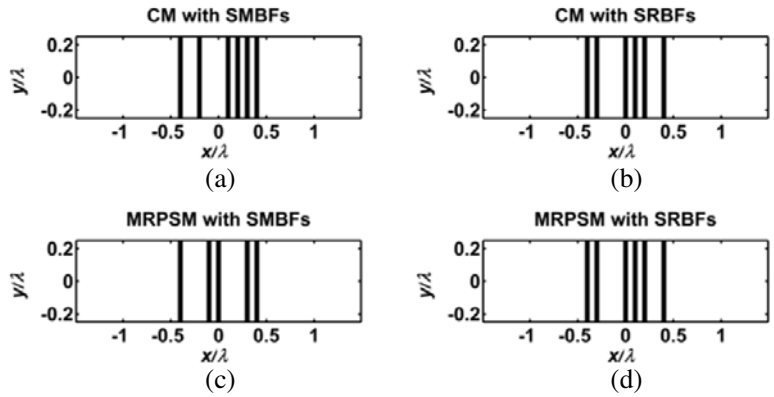

Figure 6. Recovered results by (a) CM with SMBFs; (b) CM with SRBFs; (c) MRPSM with SMBFs; and (d) MRPSM with SRBFs; black strips represent the PEC strips.

In the CM, the number of combinations is 512. In the MRPSM, we set N_{LAR} to be 9.

It can be seen from Figs. 6(a) and (c)that the results are not very accurate when we use SMBFs in the CM or MRPSM, although the SMBFs method is 8 times faster. In contrast to this, it can be seen from Figs. 6(b) and (d) that the images are faithful reproductions of the object (array of strips) when we use SRBFs in the CM or MRPSM, albeit at an increased computational cost. The reason is that the SRBFs provide a better numerical representation of the current distribution over the strips.

Next, we consider the case of 15 PEC strips that are located at the following x-positions: $(-20, -15, -10, -9, -8, -7, -6, 0, 3, 12, 13, 14, 15, 16, 20) \times \lambda/10$, respectively, as shown in Fig. 7(d). These 15 PEC strips are illuminated by a *TE*-polarized plane wave, whose incidence angle is ($\theta = 45°$, $\varphi = 0°$). The minimum separation distance between the strips is $\lambda/10$. The image region is larger than 4λ, as may be seen from Fig. 7(c); hence, the CM would not be as efficient in this case as it was in the previous example, even if we use parallel computing techniques to help reduce the computational burden to some extent. However, due to its inherent characteristics, the MRPSM is suitable for the case where the image region is wide, even though its computational complexity increases as we increase the width of the image region.

From the previous discussion, we see that the SMBFs have better efficiencies than the SRBFs, while the SRBFs have better accuracy in comparison to the SMBFs. In view of this, we propose a combination scheme, which begins with MRPSM with SMBFs for the initial estimation and follows this up with the final refinement by utilizing a combination of the MRPSM with SRBFs. Thus, combing the advantages of both the SMBFs and SRBFs methods, this approach can not only generate the primary results faster, but can also refine it to achieve a more accurate and reliable result with greater efficiency.

Figure 7(a) shows the results for the simulated E_y field distribution derived by using FEKO, observed over an area of $20\lambda \times 20\lambda$ in the measurement plane. Fig. 7(b) shows the recovered image generated directly by utilizing the PC, and it shows that the distribution of the sources is comprised of several clusters. Fig. 7(c) shows the $y = 0$ cut of the normalized field distribution at the image plane, and the image region ranges from $-22\lambda/10$ to $23\lambda/10$ when we set the threshold δV to be 0.5. This image region contains 46 unknown units, i.e., $N_{IR} = 46$; and we set N_{LAR} to be 9. Fig. 7(e) shows that the MRPSM applied by using the joint method generates a final recovered result, which is a faithful reproduction of the original distribution, as shown in Fig. 7(d). In addition, we compare the running times of the MRPSM with SMBFs, SRBFs, and joint method, and we find that the MRPSM with SMBFs is 6 times faster than that with SRBFs, and the MRPSM with joint method is 2 times faster than that with SRBFs. In conclusion, the combination of MRPSM with SMBFs is the fastest approach, but it does not produce an accurate result. In contrast to this, the SRBFs and the joint method can recover the image results with good fidelity, although at an increased cost. To summarize, the MRPSM offers good combination of efficiency and accuracy when combined with the joint method.

We now turn to the issue of the SNR of the measured data. Fig. 8 shows the numerical results for different levels of SNR of the measured data (SNR_M) in the presence of additive Gaussian white

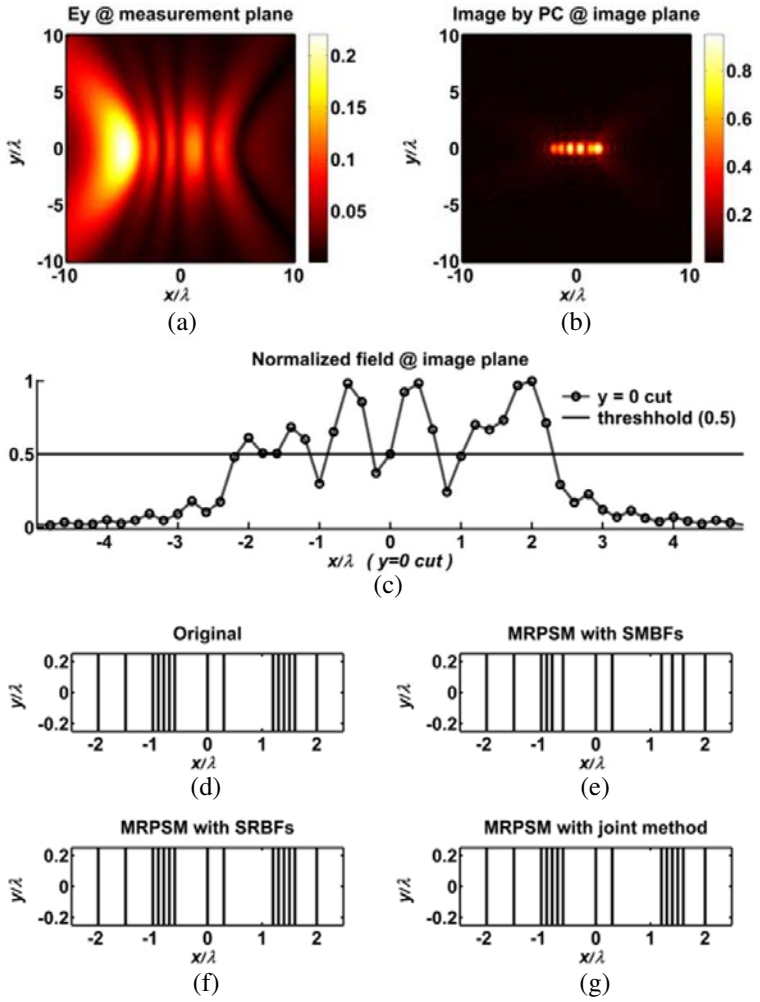

Figure 7. (a) E_y field distribution at the measurement plane; (b) image recovered by PC at the image plane; (c) normalized magnitude of E_y at the image plane ($y = 0$ cut); (d) original source distribution; and recovered results by (e) MRPSM with SMBFs, (f) MRPSM with SRBFs, and (g) MRPSM with joint method; black strips represent the PEC strips.

noise. Figs. 5–8 demonstrate that both the CM and the MRPSM can achieve a $\lambda/10$ sub-wavelength resolution relatively efficiently when the image region is not wide. On the other hand, for the case when the image region is wide, the joint version of the MRPSM method,which combines the advantages of both SMBFs and SRBFs, produces accurate and reliable results with good efficiency. Specifically, such a joint approach can reliably achieve a sub-wavelength resolution of $\lambda/10$ even when the image region is wide.

It is important to point out that in practice the local adjustment region N_{LAR} needs to be carefully chosen for a complex model. For instance, a larger value of N_{LAR} may unnecessarily increase the computational complexity, while a value of N_{LAR} which is too small could reduce the accuracy of the results, because the mutual coupling effects may not be modeled sufficiently accurately.

2.1.4. Sparse Reconstruction Method

The microwave sub-wavelength imaging problem can be treated as a sparse reconstruction problem when the distribution of the targets is sparse, and it may be stated as follows: Find the positions and amplitudes of the excitation sources from the measured data and the characteristics of the given system.

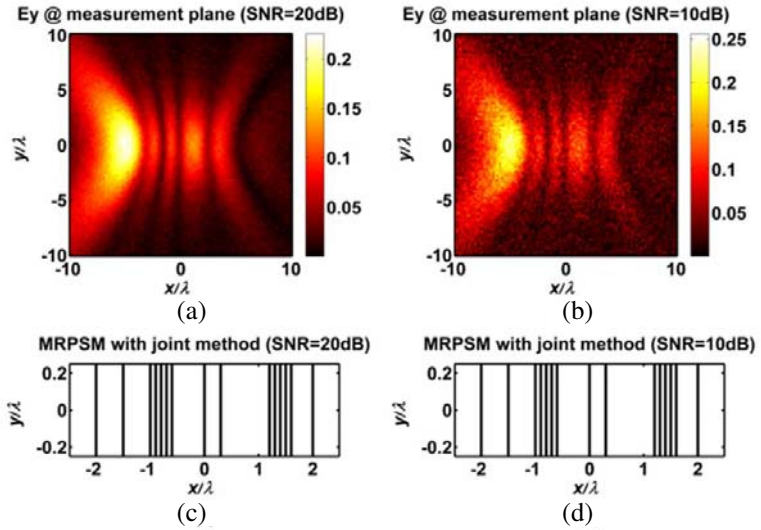

Figure 8. E_y field distribution at the measurement plane when (a) $SNR_M = 20\,\text{dB}$, (b) $SNR_M = 10\,\text{dB}$; recovered results by MRPSM with joint method when (a) $SNR_M = 20\,\text{dB}$, (b) $SNR_M = 10\,\text{dB}$; black strips represent the PEC strips.

Here, we propose the some sparse reconstruction algorithms, which are used in Compressive Sensing (CS) [34], for this problem.

The microwave sub-wavelength imaging model is essentially constructed based on the fields radiated by objects acting as secondary sources, e.g., different types of dipoles or perfectly conducting strips that are illuminated by a plane wave. Without loss of generality, we assume that the objects we are dealing with are half-wavelength dipoles. The induced current distribution on such dipoles can be approximated as follows:

$$\hat{I}(y) = \begin{cases} \hat{a}_y I_m \sin\left[k\left(\dfrac{l}{2} - y\right)\right] & \left(0 \le y \le \dfrac{l}{2}\right) \\ \hat{a}_y I_m \sin\left[k\left(\dfrac{l}{2} + y\right)\right] & \left(-\dfrac{l}{2} \le y < 0\right) \end{cases} \tag{8}$$

where $I_m = constant$ is the magnitude of the exciting current, l is the length of the dipole.

According to [35], we can calculate the E_y field distribution as follows:

$$E_y = -jI_m \frac{\eta}{4\pi}\left[\frac{e^{-jkR_1}}{R_1} + \frac{e^{-jkR_2}}{R_2} - 2\cos\left(\frac{kl}{2}\right)\frac{e^{-jkr}}{r}\right] \tag{9}$$

where R_1 and R_2 are the distances from the end points of the dipole to the observation point, and r represents the distance from the central point of the dipole to the observation point.

We can establish the relationship between the measured data and the current distribution of the sources in a matrix form as:

$$\mathbf{E} = \mathbf{A} \cdot \mathbf{I} \tag{10}$$

where $\mathbf{E}$ represents the measured data vector which is consisted of E_y-component, $\mathbf{A}$ is the system matrix and $\mathbf{I}$ is the source distribution vector.

We employ SRBFs to simulate the field distribution scattered by 10 PEC strips located along the x-direction, whose lengths and widths are $\lambda/2$ and $\lambda/20$, respectively. A plane wave, which propagates perpendicularly to the source plane with its electric field polarized along the y-direction, is incident upon these strips. We set the operating frequency to be 10 GHz. We assume that the induced current is sinusoidal in the y-direction and constant along the x-direction. The scattered electric field is measured at a distance $d = \lambda$ from the source plane,the spatial sampling rate at the measurement plane is $\lambda/10$, the number of samples is 101 and the aperture size is 10λ. The strips are centred at $(-10, 8, 5, 4, 3, 0, 3, 5, 7, 9) \times \lambda/10$ along the x-direction, respectively.

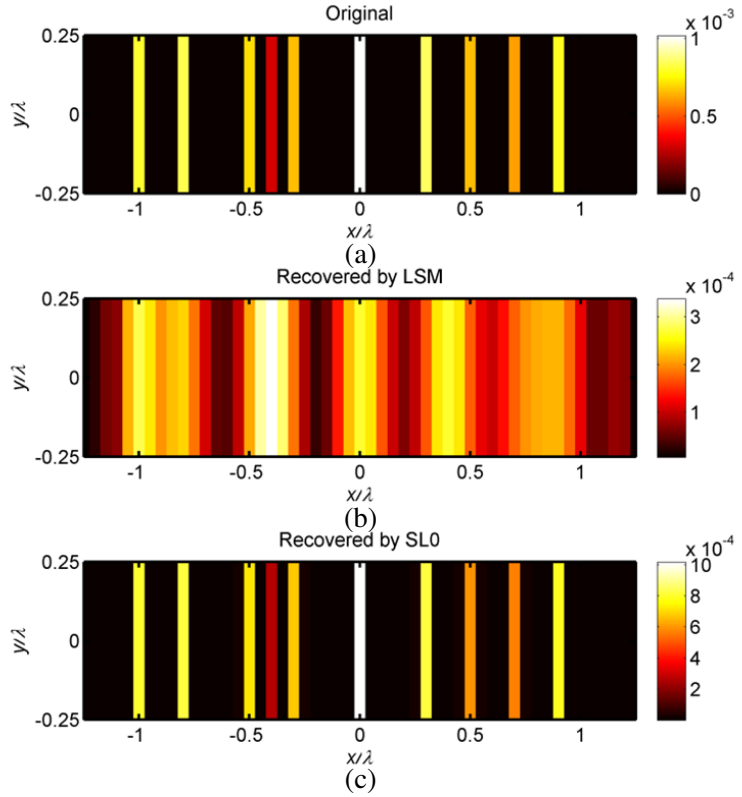

Figure 9. (a) Original distribution of strips; (b) image recovered by LSM; and (c) image recovered by SL0.

Figure 9(a) shows the original distribution of the strips, where the bright bands represent the PEC strips with different induced current magnitudes. Instead of, Fig. 9(b) shows the image recovered by the Least Square Method (LSM), while Fig. 9(c) shows the recovered image obtained by using the Smoothed l_0 algorithm (SL0) [36]. The least square method is a widely used approach for solving inverse problems. However, it is difficult to achieve an accurate solution by using this method, since the condition number of the system matrix $\mathbf{A}$ is very large, and the rank of $\mathbf{A}$ is much less than the number of unknowns. For this reason, we use the smoothed l_0 algorithm, which was originally developed for sparse reconstruction in CS, to find the sparse solutions of an underdetermined system of linear equations.

Although the performance of this algorithm is good, it is sensitive to noise because of the ill-conditioned nature of the system matrix $\mathbf{A}$ and its final optimization results depend on a good initial guess.

2.2. Multi-Dimensional Microwave Sub-wavelength Imaging

2.2.1. Microwave Sub-Wavelength Imaging for Transverse and Longitudinal Distributions

Figure 10 shows the representative scheme for imaging systems using phase conjugating lenses with transversely and longitudinally distributed targets. The test objects are PEC squares that are illuminated by an incident plane wave. At the measurement plane, the phase conjugation lens collects the scattered field; phase conjugates this field and propagates it to the image plane to form the image.

For the transverse case, the distance between the source and measurement planes is fixed to d, and the distance between the image and measurement planes is also fixed to d (in Fig. 10(a)). However, for the longitudinal case, the PEC squares are located along the z-axis, and the image plane is shifting along the z-axis in the image region (in Fig. 10(b)).

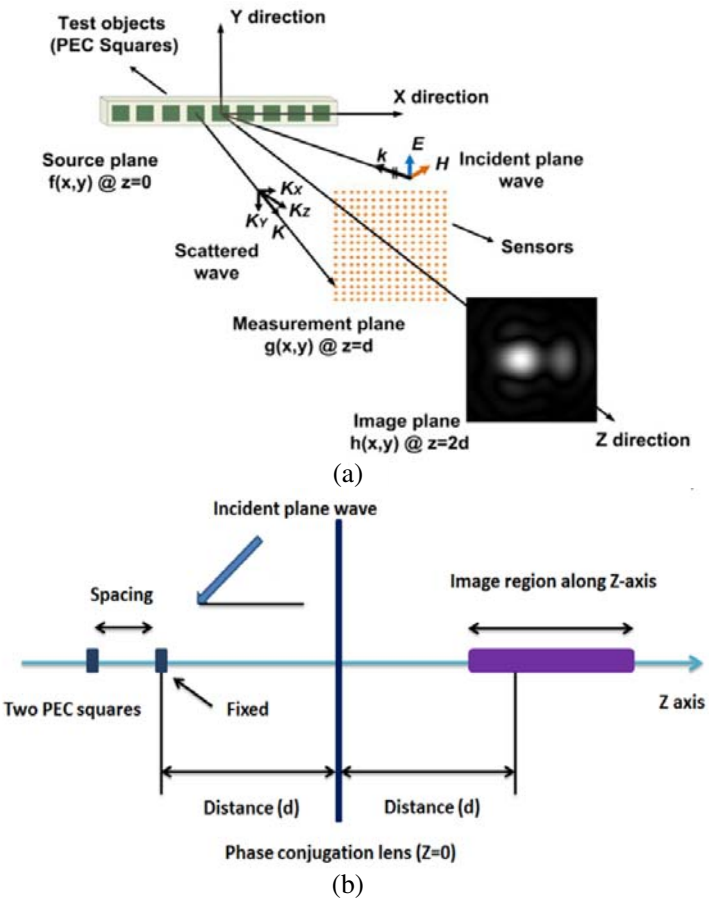

Figure 10. Schematic for microwave sub-wavelength imaging using PC lens with the objects located along (a) transverse axis (x-axis), (b) longitudinal axis (z-axis).

2.2.2. SVD-based Basis Matrix Method

Next, we describe an imaging algorithm based on the Singular-Value-Decomposition (SVD)-based basis matrix method. As a starter, we use the FEKO 6.2 Suit to simulate the case of a single PEC square at a time, which is located in the source plane. We derive the scattered field distribution in the measurement plane, phase conjugate it, and then let it propagate to the image plane. Finally, we extract a part of the image distribution, for instance its values along the $y = 0$ cut to form a column of the basis matrix. The number of the columns in this matrix corresponds to the number of possible positions for the PEC square in the source plane. We then apply a SVD-based basis matrix method to it, and use a threshold to delete the singular vectors, whose singular value fall below the threshold.

The step-by-step procedure can be summarized as follows:

1) Locate one PEC square in the "possible" position at one time, and extract a part of the image distribution, for instance its values along the $y = 0$ cut.
2) Create the basis matrix by using the extracted values obtained in the previous step, and the number of the columns in this matrix corresponds to the number of possible positions for the PEC square in the source plane.
3) The basis matrix is written as $\mathbf{B}_{(N\times M)}$. Hence, we can generate an equation as follows:

$$\mathbf{e}_{N\times 1} = \mathbf{B}_{N\times M} \cdot \mathbf{x}_{M\times 1} \tag{11}$$

where $\mathbf{B}_{(N\times M)}$ represents the basis matrix, and N is the number of the extracted values and M is

the number of possible positions for the PEC square in the source plane. Here $\mathbf{e}_{(N\times 1)}$ represents the "measured" values, and $\mathbf{x}_{(M\times 1)}$ represents the possible targets.

4) Equation (11) usually represents an ill-posed problem. Hence, we apply the SVD to the basis matrix, i.e., to derive $\mathbf{B} = \mathbf{UDV}$, and use a threshold level to reduce the matrix by deleting the singular vectors whose singular values fall below the threshold.

5) Take a dot product of the K ($K < M$) remaining singular vectors $\mathbf{U}_{(N\times K)}$ with the "measured" values, as well as the basis matrix, to obtain a reduced vector $\mathbf{e}^n_{(K\times 1)}$ and a reduced matrix $\mathbf{B}^n_{(K\times M)}$.

$$\mathbf{e}^n_{K\times 1} = \mathbf{B}^n_{K\times M} \cdot \mathbf{x}_{M\times 1} \tag{12}$$

6) Unlike (11), (12) represents a well-conditioned problem, and the size of the associated basis matrix $\mathbf{B}^n_{(K\times M)}$ is significantly reduced compared to that in (11). Hence, we directly pseudo-inverse the reduced basis matrix $\mathbf{B}^n_{(K\times M)}$ and take its product with the reduced vector $\mathbf{e}^n_{(K\times 1)}$ to derive the final results.

In the simulation for the transverse case, we set the size of the PEC square to be $\lambda/20 \times \lambda/20$, and the spacing to be $\lambda/4$ in both the x- and y-directions. The distance between the source and measurement planes is 3λ. The size of the measurement aperture is $30\lambda \times 30\lambda$ with $\lambda/20$ interval in both x- and y-directions. And the size of the image zone is $10\lambda \times 10\lambda$ with $\lambda/4$ interval in both x- and y-directions. The operating frequency is 1 GHz, and the plane wave is normally incident.

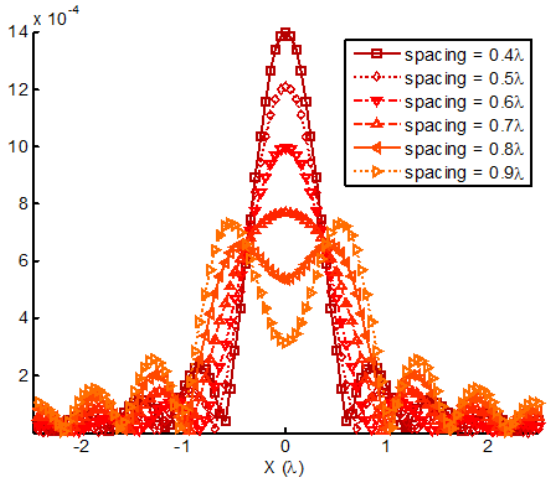

Figure 11. Raw image (field distribution) results obtained by using the PC lens when two objects are located in the transverse plane along the x-axis, and their spacing is varied from $2\lambda/5$ to $9\lambda/10$, with a $\lambda/10$ step.

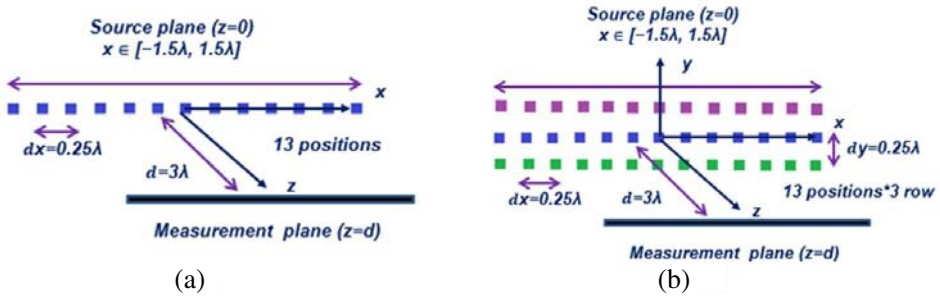

Figure 12. Imaging models for (a) 1D case (x-direction); and (b) 2D case (x-y plane).

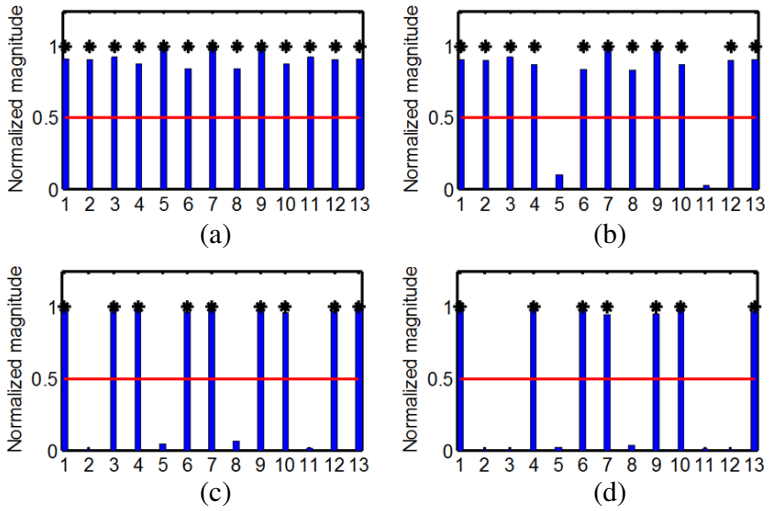

Figure 13. Imaging results for the 1D case (x-direction) via the SVD-based basis matrix method.

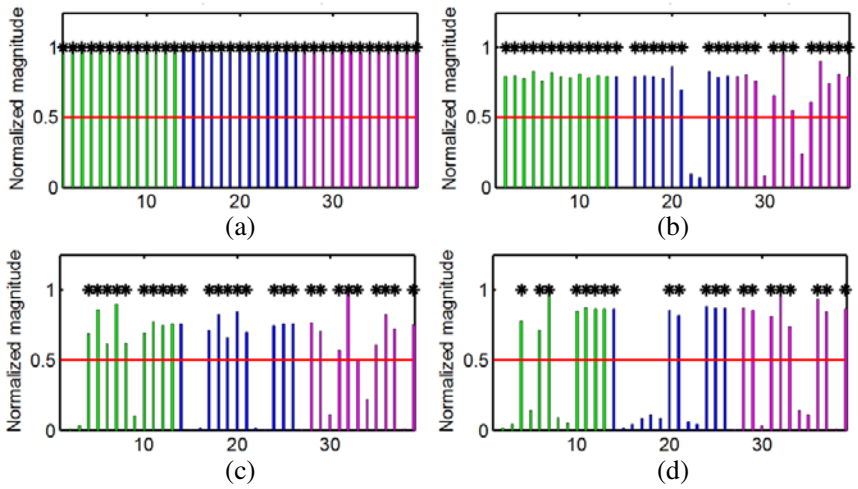

Figure 14. Imaging results for the 2D case (x-y plane) via the SVD-based basis matrix method.

Figure 11 shows the raw image (field distribution) results obtained by using the PC lens when two objects are located in the transverse plane along the x-axis, and their spacing is varied from $2\lambda/5$ to $9\lambda/10$, with a $\lambda/10$ step. From Fig. 11, it is obvious that with the increase of the spacing, the two PEC squares can be separated more easily.

Figure 12 shows the imaging models for the 1D and 2D cases. The basis matrices are comprised of 13 and 39 columns, respectively. The source zone in the x-direction ranges from $-15\lambda/10$ to $15\lambda/10$. Figs. 13 and 14 show the recovered results for the 1D and 2D cases; respectively, the stars and the bars represent the original and the recovered positions of PEC squares; respectively, and the horizontal line at the level of 0.5 (normalized) is used to distinguish the real objects from the false ones. Here, we have set a threshold of 10^{-5} for the truncation of the singular values. For the 1D case (x-direction), we only extract $y = 0$ cut to generate the basis matrix, and that find 13 singular vectors survive. For the 2D case(x-y plane), we use three cuts e.g., at $y = (-1, 0, 1) \times \lambda/10$, and 35 singular vectors are survived. From Figs. 13 and 14, we see that the basis matrix method applied in conjunction with the SVD is capable of accurately recovering the position of the object.

For the longitudinal case, we set the size of the PEC square to be $\lambda/20 \times \lambda/20$, and let the spacings in the z-direction to range from $3\lambda/10$ to 2λ. The distance between the source and measurement planes

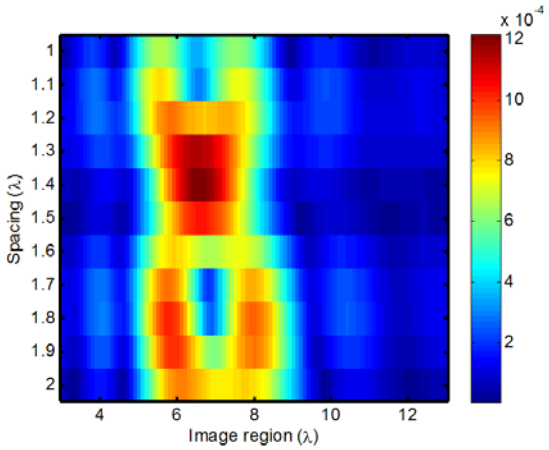

Figure 15. Raw image (field intensity) results obtained by using the PC lens when two objects are located along the longitudinal axis (z-axis): region from 1λ to 2λ with a $\lambda/10$ step.

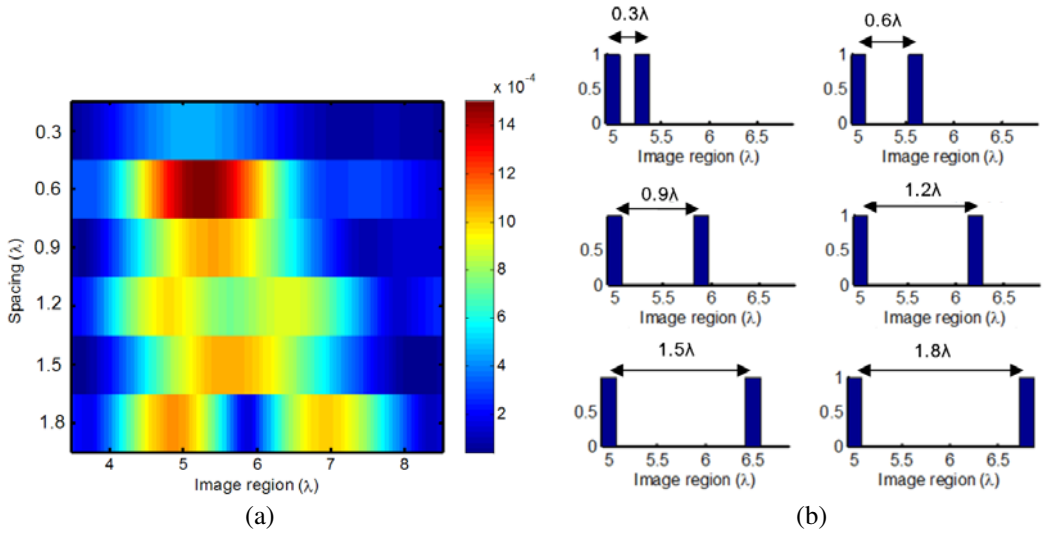

Figure 16. Image results (field distribution) obtained by using a PC lens when two objects are located along the longitudinal axis (z-axis) and the spacing between them is varied: (a) raw images (field distribution) before processing; (b) results after processing the raw images by using the proposed technique.

is 3λ. The size of the measurement aperture is $30\lambda \times 30\lambda$ with $\lambda/20$ interval in both x- and y-directions. And the size of the image zone is $10\lambda \times 10\lambda$ with $\lambda/4$ interval in both x- and y-directions. The operating frequency is 1 GHz, and the plane wave is normally incident.

Figure 15 shows that the longitudinal case is quite different from the transverse case, we keep one PEC square's position unchanged, and shift the other PEC square to the negative longitudinal axis, the space is from 1λ to 2λ with a $\lambda/10$ step. It shows that the raw image of the two PEC squares merges twice with an increase of the spacing when the spacing is 1.4λ and 2λ, while the image retains its separation in the transverse case. Fig. 16 shows the recovered results for the longitudinal case — The bars represent the recovered positions of PEC squares and we can see that the SVD-based basis matrix method also works in the longitudinal case

It is evident from the results presented above that the SVD-based basis matrix method can enhance the resolution of the images generated by a PC lens quite considerably, both in the longitudinal and transverse separation cases

3. LUNEBURG LENS ANTENNAS FOR DIRECTION-OF-ARRIVAL ESTIMATION

3.1. Direction-of-Arrival Estimation with Normal Luneburg Lens Antenna

The Luneburg lens is designed to focus a plane wave, arriving from an arbitrary direction, at a point which is located diametrically opposite to that of the incident side. Luneburg has shown that the problem of finding ε_r of the lens can be formulated in terms of an integral equation [25], whose solution provides us the required material parameters of the lens. They are given by:

$$\varepsilon_r = 2 - (r/R)^2 \tag{13}$$

where r is the distance from the center of the lens, and R is its radius.

Next, we introduce the principles of sparse reconstruction algorithms to analyze the normal Luneburg lens antenna. Without loss of generality, we consider a 1D DOA case, in which there is only one degree of freedom for the incident angle. To realize it, we fix the incident angle φ and only vary θ. We distribute the sensors on the curved surface of the Luneburg lens in a uniform manner and use these sensors to measure the electric field at their locations. According to the concepts of the sparse signal representation, we generate the relationship between the unknown incident angle vector $\mathbf{x}(M \times 1)$ and the measured data vector $\mathbf{y}(N \times 1)$, where M is the number of possible incident angles and N is the number of sensors. The matrix $\mathbf{A}(N \times M)$ is comprised of training data, which is collected or simulated for each possible incident angle and is known *a priori*. Hence, the DOA problem with additive white Gaussian can be stated as:

$$\mathbf{y} = \mathbf{A}\mathbf{x} + \mathbf{n} \tag{14}$$

where $\mathbf{n}(N \times 1)$ represents the noise vector.

The l_1-norm objective function for (14) can be written as:

$$\min \|\mathbf{x}\|_1 \quad \textit{subject to } \|\mathbf{y} - \mathbf{A}\mathbf{x}\|_2^2 \le \beta^2 \tag{15}$$

where β is a parameter specifying an allowable noise level.

We use a commercial Finite Difference Time Domain (FDTD) [38] code to simulate the antenna geometry. We set the interval between the sensors to be 5°, and we arrange 37 ($N = 37$) sensors on the surface of the Luneburg lens. The number of possible incident angles is set to be 361 ($M = 361$, $-90° < \theta < 90°$). Since the Luneburg lens is spherically symmetric, we only simulate the problem for one incident angle, collect the electric field and rotate it by a 0.5° step ($\Delta\theta = 0.5°$). The incident plane waves are assumed to arrive from 7 different directions. Their incident angles and normalized coefficients are: (62.6°, $0.48e^{j79°}$), (−6.3° , $1.00e^{-j57°}$), (−9.4°, $0.77e^{j14°}$), (−44.4°, $0.20e^{j64°}$), (−49.7°, $0.17e^{-j84°}$), (−54.2°, $0.51e^{-j85°}$) and (−71.3°, $0.83e^{j65°}$). We assume the frequency to be 8 GHz though it can be easily changed, and we set the SNR to be 30 dB. We apply the algorithm for large-scale sparse reconstruction (SPGL1) [37] to the measured data for the l_1-norm sparse reconstruction. The recovered results obtained by using the CM and the SPGL1 algorithms are shown in Fig. 17.

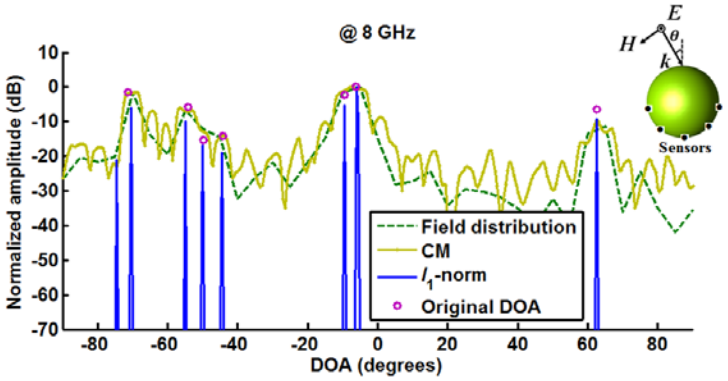

Figure 17. Field distribution and recovered results by using CM and the SPGL1 algorithms.

Figure 17 shows that the l_1-norm sparse reconstruction algorithm, i.e., SPGL1 algorithm, has much better resolution than the CM. The highest resolution achieved by using l_1-norm sparse reconstruction algorithm is 3.1°, which is better than the angular resolution (3.5° @ 8 GHz) predicted on the basis of the 3 dB-beamwidth concept. Although there is a ghost at −75° with a relative small magnitude (around −23 dB), considering the SNR is 30 dB, a ghost with such a low level is acceptable.

From Fig. 17, we also see that the proposed method can be utilized for wide angle scanning, even to −71.3°, and works for ultra-wideband frequency, range of 2 GHz to 12 GHz, although we have only shown the 8 GHz case.

3.2. Direction-of-Arrival Estimation with Flat-Base Luneburg Lens Antenna

3.2.1. Design of Flat-Base Luneburg Lens Antenna

In [29], we have proposed a design, shown in Fig. 18, of a lens with a spherical profile, which preserves the salutary features of the conventional Luneburg lens but is much more convenient to feed in the transmit mode since it has a flat-base design. In this section, we consider its advantages in DOA estimation by using signal processing techniques

As shown in Fig. 18, the Luneburg lens consists of 11 layers and has a diameter of 63.5 mm. The first ten layers from the center have a thickness of 3 mm each and the last layer is 1.75 mm thick. The dielectric parameters of the layers vary depending on their distance from the center, in accordance with (13). The flat-base is a 6×6 waveguide array with PEC walls that are 1 mm thick. The waveguide has a square cross-section with a side length of 9 mm. We set an array of observers in the measurement plane, i.e., the truncation plane of the waveguides.

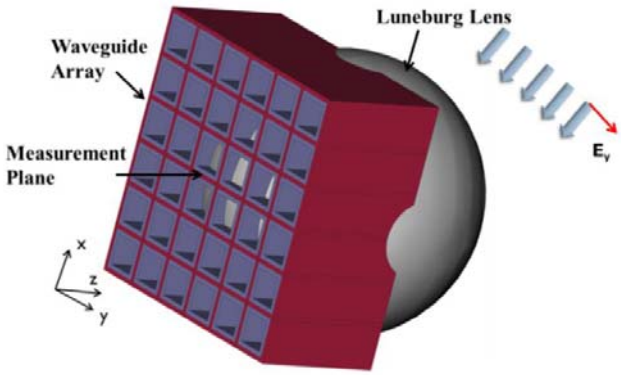

Figure 18. Flat-base Luneburg lens antenna for DOA estimation.

It is well-known that the angular resolution of an antenna is determined by its half-power beam-width, which is inversely proportional to the aperture size of the antenna. We calculate the half-power beam-width of the Luneburg lens as λ/D by assuming the aperture efficiency is unity, where λ is the free space wavelength and D is the diameter of the Luneburg lens. This is slightly larger than 9° for a diameter of $D = 63.5$ mm at 30 GHz.

3.2.2. Correlation Method

To enhance the resolution of the above Luneburg lens, we propose to employ the Correlation Method (CM). In the following section we describe the case based on CM to detect multiple targets with different incident angles and different Radar Cross Section (RCS) levels. We develop the measurement database, comprising of the electric fields in the measurement plane that is induced by targets that have different combinations of orientations, distances and scattering cross-sections. Thus, the measurement database is derived by doing a vector addition of the field distributions due to the individual targets located at different angles.

The CM is based on correlating the measured field distribution in the measurement plane due to an unknown distribution of targets with all the entries in the measurement database. The correlation coefficient (ρ_n) for the n-th entry in the database is defined as:

$$\rho_n = \frac{1}{(M_i M_j - 1)\sigma^M \sigma_n^D} \sum_{i=1}^{M_i} \sum_{j=1}^{M_j} \left[\left(E^M(x_i, y_j) - \mu^M \right) \left(E_n^D(x_i, y_j) - \mu_n^D \right)^* \right] \tag{16}$$

where the superscript 'M' denotes the field distribution in the measurement plane induced by the targets; the superscript 'D' denotes the known field distribution in the measurement plane, which is stored in the database; and μ and σ refer to the mean and standard deviation of the field distribution; respectively. Also, M_i and M_j are the number of sample points in the measurement plane along x- and y-directions, respectively. The value of n that maximizes ρ determines the angular locations of the targets, as well as their relative RCSs.

The scattered field from a target which is being interrogated by the antenna operating in the receive mode can be treated as a plane wave incident up on the antenna from the direction of the target, and we also use a commercial Finite Difference Time Domain (FDTD) code to simulate the antenna geometry, shown in Fig. 18, to obtain the field distribution in the measurement plane. We do this for a y-polarized unit amplitude plane wave for 16 different incident angles, given by $\varphi = 0^\circ$ and θ varying from 30° to 45° with an interval of 1°, and we set the observation frequency to be 30 GHz.

We next investigate the case of two targets with very small angular separation, i.e., less than half-power beam-width. The two angles were randomly chosen from 30° to 45° in θ with $\varphi = 0^\circ$, and their combined electric field distributions in the measurement plane were derived by using random amplitude scaling factor in the range of [0.4, 2.5] and random initial phases in the range of [0°, 359°]. We consider 50 random pairs of incident plane waves. If there is only one target it would correspond to the case when first and second angles are the same. The total fields measured in the measurement plane can be expressed as:

$$E_{total} = a_1 e^{j\phi_1} E_1 + a_2 e^{j\varphi_2} E_2 = a_1 e^{j\phi_1} \left(E_1 + \frac{a_2}{a_1} e^{j(\phi_2 - \phi_1)} E_2 \right) \tag{17}$$

where E_1 and E_2 are the known electrical fields measured in the measurement plane when uniform plane waves with unit amplitudes are incident on the lens from two different directions. Also, (a_1, $\emptyset_1$) and (a_2, $\emptyset_2$) are the amplitude scales and initial phases of the fields scattered by the first and second randomly chosen scatterers, respectively.

In the CM approach, the field distributions in the measurement plane are then correlated with those in the measurement database. The highest value of correlation coefficient estimates the angular location of the targets and their characteristics. We consider the step of the amplitude scaling factor (a_2/a_1) as: 1, 1.25, 1.5, 1.75, 2.0, 2.25, 2.5, 1/1.25, 1/1.5, 1/1.75, 1/2.0, 1/2.25 and 1/2.5; we also consider the step of the difference of phase ($\emptyset_2$-$\emptyset_1$) as: 0°, 9°, 18°, ..., 351°. We note that, for a pair of incident angles, with an amplitude step of 0.25 and phase step of 9°, it is necessary to consider a total of $16 \times 16 \times 10 \times 40$ different combinations that are obtained if we take a combination of 10 cases for the amplitude scaling factor (a_2/a_1), and 40 for the initial phase difference ($\emptyset_2$-$\emptyset_1$).

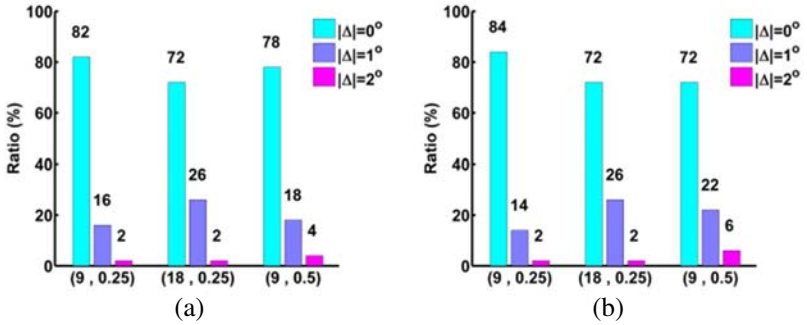

Figure 19. Accuracy ratios for first (a) and second (b) incident angle with different search steps: (i) $\delta\emptyset = 9^\circ$ and $\delta a = 0.25$, (ii) $\delta\emptyset = 18^\circ$ and $\delta a = 0.25$, and (iii) $\delta\emptyset = 9^\circ$ and $\delta a = 0.5$.

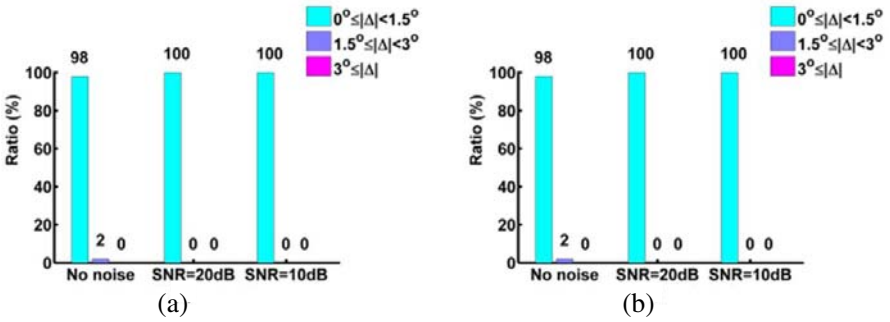

Figure 20. Accuracy ratios in the estimation results for the first (a) and second (b) incident angle for different SNR with 18 samplings at each waveguide truncation plane.

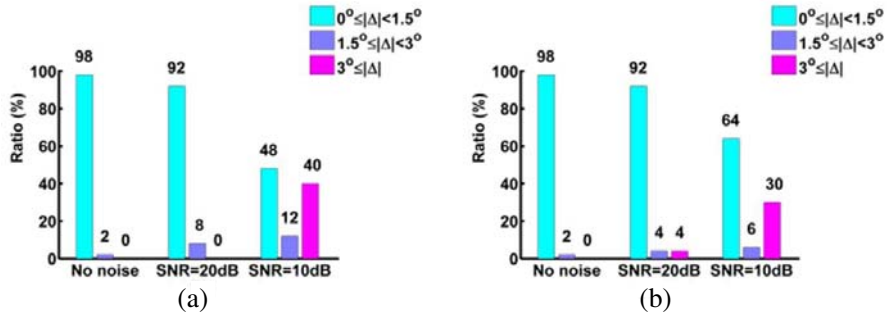

Figure 21. Accuracy ratios in the estimation results for the first (a) and second (b) incident angle for different SNR with 9 samplings at each waveguide truncation plane.

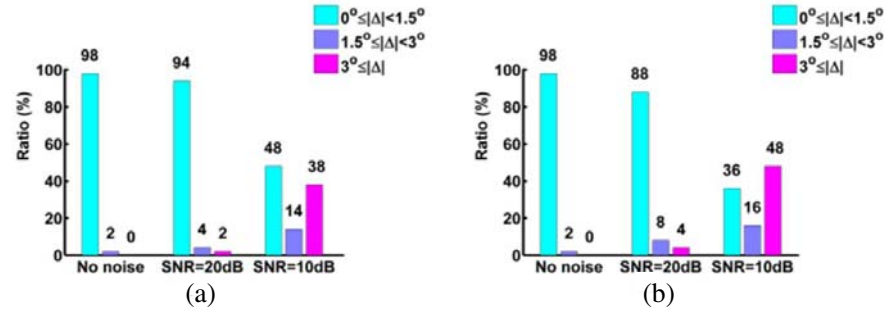

Figure 22. Accuracy ratios in the estimation results for the first (a) and second (b) incident angle for different SNR with 4 samplings at each waveguide truncation plane.

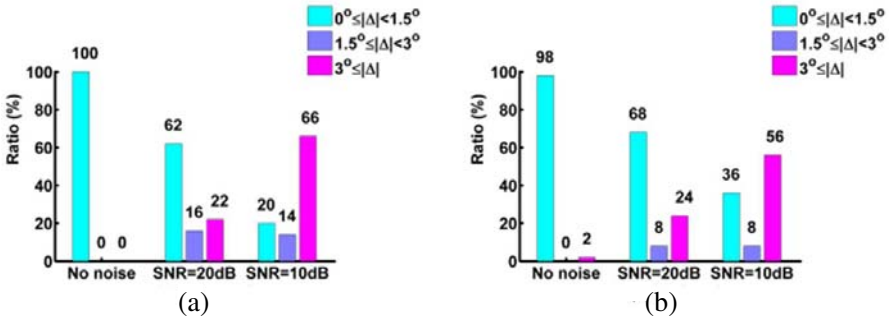

Figure 23. Accuracy ratios in the estimation results for the first (a) and second (b) incident angle for different SNR with 1 sampling at each waveguide truncation plane.

Next, we determine the optimal combination of the amplitude scale step (δa) and the phase difference step ($\delta\emptyset$) to achieve a high resolution. Three different δa and $\delta\emptyset$ combinations are considered, namely (i) $\delta\emptyset = 9^\circ$ and $\delta a = 0.25$; (ii) $\delta\emptyset = 18^\circ$ and $\delta a = 0.25$; and (iii) $\delta\emptyset = 9^\circ$ and $\delta a = 0.5$. Fig. 19 shows the percentage accuracy for these three cases, computed by using the 50 random pairs of targets in the absence of noise. As expected, the smaller the amplitude scale and phase difference steps, the higher the accuracy we can achieve. In all cases, the angular error in the detection is less than 2°. Also, we note that using (i) results in more accurate estimation at the cost of higher computational complexity. Hence, we can choose $\delta\emptyset = 9^\circ$ and $\delta a = 0.25$ to construct the measurement database.

Figures 20–23 show the accuracy ratios for the 50 pairs of incident plane waves, for different SNRs and for 18, 9, 4 and 1 field sampling points; respectively, in the x- and y-directions for each waveguide in the measurement plane, using search steps of $\delta\emptyset = 9^\circ$ and $\delta a = 0.25$. It is evident that the target estimation accuracy is more susceptible to noise when the number of field sampling points is lower. However, since it is difficult to measure the fields at a large number of points in a waveguide in practical scenarios, we must resort to a compromise between the target detection accuracy and the number of sampling points. Also, as the SNR decreases to 10 dB, percentage target estimation accuracies achieved are 100%, 50%, 40% and 30%, for 18, 9, 4 and 1 sample, respectively. But, the SNR of a typical radar system can be kept well above 20 dB. Therefore, for a SNR above 20 dB, we are able to achieve percentage target estimation accuracies of 100%, 92%, 91% and 65% by using 18, 9, 4 and 1 sample, respectively.

3.2.3. Waveguide Mode Extraction and SVD-Based Basis Matrix Method

In Subsubsection 3.2.1, a spherical Luneburg lens antenna with a planar waveguide array has been proposed. To enhance the angular resolution of the lens antenna, we propose a waveguide mode extraction technique followed by the use of signal processing techniques. We begin by sampling the electric field at the cross-section plane of the waveguide array and then extracting the weights of the possible propagating modes in each waveguide. Next, we apply the CM to obtain an initial estimate of the possible DOAs. Following this, we employ an SVD-based basis matrix method to achieve a more precise estimate of the DOAs.

Next, we detail the procedure for waveguide mode extraction. The cutoff frequencies of the electromagnetic waveguide can be complied from [39]:

$$f_{cutoff}(m,n) = \frac{1}{2\sqrt{\mu\varepsilon}}\sqrt{\left(\frac{m}{a}\right)^2 + \left(\frac{n}{b}\right)^2} \tag{18}$$

where a and b represent the dimensions of the waveguide aperture at the transverse (x-y) plane; ε and μ are the permittivity and permeability of the medium inside the waveguide, respectively; and the integers m and n indicate different modes.

We set the operating frequency to be $f = 30$ GHz and choose the side dimensions of each square waveguide to be $a = b = 9$ mm. The cutoff frequencies for TE_{10}, TE_{01}, TE_{11} and TM_{11} modes are calculated using (18) and are found to be 16.67 GHz, 16.67 GHz, 23.57 GHz, and 23.57 GHz, respectively.

Once the possible modes are known, the field distribution on the face of each waveguide can be expressed as a weighted sum of the field distributions for these possible modes as follows:

$$\vec{\mathbf{E}} = \mathbf{c_1}\vec{\mathbf{E}}^{\mathbf{TE_{10}}} + \mathbf{c_2}\vec{\mathbf{E}}^{\mathbf{TE_{01}}} + \mathbf{c_3}\vec{\mathbf{E}}^{\mathbf{TE_{11}}} + \mathbf{c_4}\vec{\mathbf{E}}^{\mathbf{TM_{11}}} \tag{19}$$

where c_i ($i = 1$, 2, 3 and 4) are the weights of each mode and $\vec{\mathbf{E}}^{TE_{10}}$, $\vec{\mathbf{E}}^{TE_{01}}$, $\vec{\mathbf{E}}^{TE_{11}}$ and $\vec{\mathbf{E}}^{TM_{11}}$ are the bases corresponding to field distributions for TE_{10}, TE_{01}, TE_{11} and TM_{11} modes, respectively. The field distributions corresponding to the possible modes form a complete set of orthogonal bases; hence, they can be described any set of field distributions in the waveguide under consideration.

The weights can be related to the sampling data $\vec{\mathbf{E}}$ in matrix form as:

$$\mathbf{E} = \mathbf{A} \cdot \mathbf{c} \tag{20}$$

The next question that needs to be addressed is how many field samples are really required inside each waveguide to derive an accurate DOA estimation. As is known from (19), for the structure and frequency range under consideration there are at most four degrees of freedom in each waveguide.

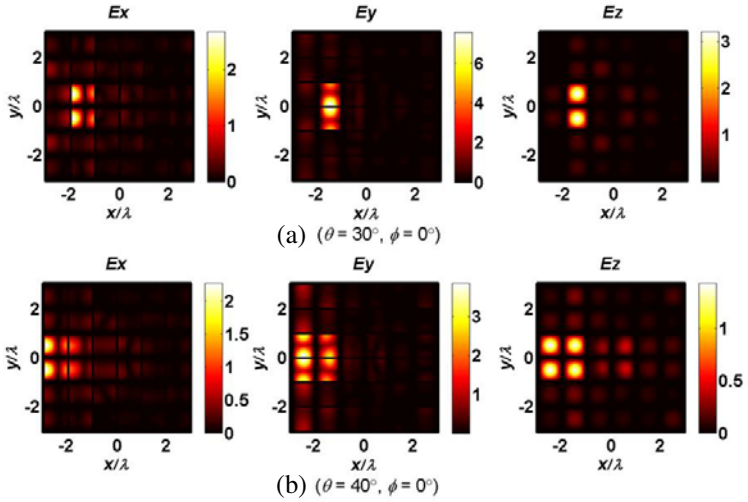

Figure 24. E-field distribution on cross-section plane of waveguide array for different incident angles: (a) $\theta = 30°$ and (b) $\theta = 40°$, with $\varphi = 0°$.

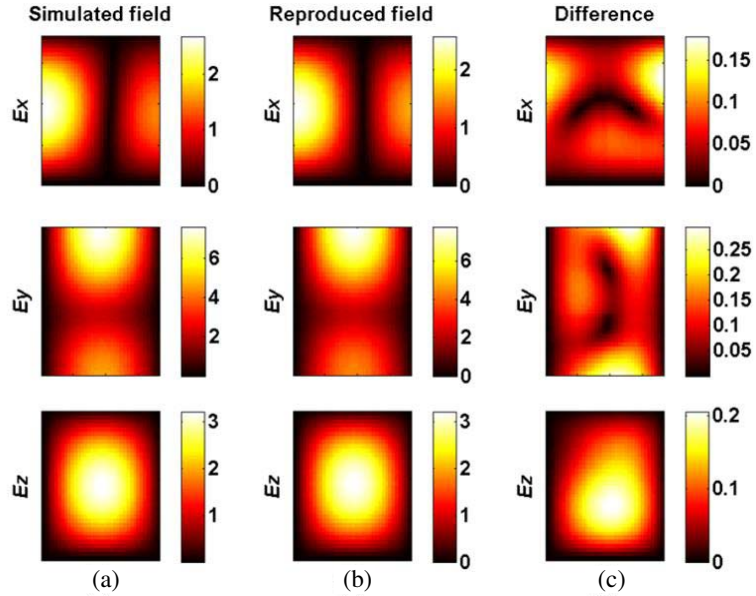

Figure 25. Comparison between simulated E-field and reproduced E-field by using waveguide mode extraction.

Viewing this issue from the perspective of the rank of the matrix $\mathbf{A}$, the maximum rank of $\mathbf{A}$ would be 2, 2 and 1, respectively, if we only measure the E_x-, E_y- or E_z-component. Hence, we should measure both E_x- and E_y-components to ensure that the matrix $\mathbf{A}$ is full-rank.

Next, we apply the CM to obtain an initial estimate of the possible DOAs. Following this we employ the SVD-based basis matrix method to achieve a more precise estimate of the DOAs. The advantage of carrying out the first step by using the CM is to narrow the search region and reduce the computational complexity. Once we have determined the approximate location of the targets, we can use the second step to achieve more accurate estimates of the DOAs.

Without loss of generality, the structure was excited with 16 y-polarized plane waves with each a unit amplitude but 16 different incident angles, corresponding to $\varphi = 0°$ and θ varying from 30° to 45°

with an interval of 1°.

Figure 24 shows the E_x-, E_y-, and E_z-field distributions on the cross-section plane for two selected incident angles. E_y is always dominant over E_x and E_z, because the incident wave is y-polarized.

Figure 25 shows a comparison between the simulated and reproduced E-fields, derived by using the waveguide mode extraction technique when $\theta = 30°$, $\varphi = 0°$. It is evident that the waveguide mode extraction technique is able to accurately calculate the weights of the propagating modes and reproduce the field distribution, with less than 10% difference between the two. The 10% error can be attributed to the evanescent modes propagating in the waveguide, since the guide is not long enough for these modes to decay completely by the time they reach the cross-section plane.

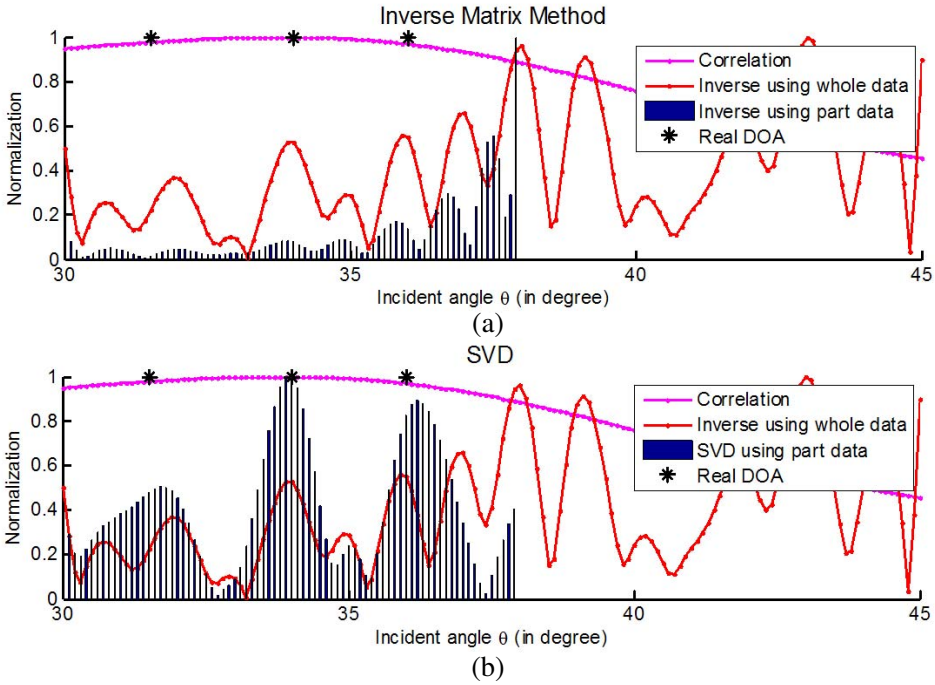

Figure 26. Recovered DOAs by using proposed method.

A case of three targets with angular separations as small as 2° was used to validate the approach. The three incident angles are set to be 31.5°, 34° and 36° in θ, with $\varphi = 0°$. From Fig. 26(a) it is obvious that the inverse matrix method and the CM are not able to recover the DOAs Fig. 26(b) shows that the proposed signal processing method can distinguish the DOAs with high accuracy even when the targets are located in angular proximity of each other Fig. 26 also shows that the recovered DOAs are very close to the real ones; however, the recovered scattering cross-sections do not match the real ones, although their magnitudes do maintain the same relative order w.r.t each other.

4. CONCLUSION

In this work, several signal processing techniques; namely the CM,the MRPSM,the sparse reconstruction method, and the SVD based basis matrix method have been presented and their abilities to resolve at a sub-wavelength level for microwave imaging and high angular resolution than the basis of the half-power beam-width of the lens antenna for DOA estimation have been examined. We show that by combining these signal processing techniques the performance for the "perfect lens"; i.e., the phase conjugation lens and Luneburg lens, will be enhanced.We believe that further research in this direction would be very fruitful and we recommend it.

REFERENCES

1. Nieto-Vesperinas, M. and E. Wolf, "Phase conjugation and symmetries with wave fields in free space containing evanescent components," *J. Opt. Soc. Amer.*, Vol. 2, No. 9, 1429–1434, 1985.
2. Pendry, J. B., "Negative refraction makes a perfect lens," *Phys. Rev. Lett.*, Vol. 85, No. 18, 3966–3969, 2000.
3. Maslovski, S. and S. Tretyakov, "Phase conjugation and perfect lensing," *J. Appl. Phys.*, Vol. 94, No. 7, 4241–4243, 2003.
4. Rosny, J. de, G. Lerosey and M. Fink, "Theory of electromagnetic time-reversal mirrors," *IEEE Trans. Antennas Propag.*, Vol. 58, No. 10, 3139–3149, 2010.
5. Shiroma, G. S., R. Y. Miyamoto, J. D. Roque, J. M. Cardenas, and W. A. Shiroma, "A high-directivity combined self-beam/null-steering array for secure point-to-point communications," *IEEE Trans. Microw. Theory Tech.*, Vol. 55, No. 5, 838–844, 2007.
6. Gaikovich, K. P., "Subsurface near-field scanning tomography," *Phys. Rev. Lett.*, Vol. 98, No. 18, 183902–183902, 2007.
7. Aliferis, I., T. Savelyev, M. J. Yedlin, J.-Y. Dauvignac, A. Yarovoy, C. Pichot, and L. Ligfhart, "Comparison of the diffraction stack and time-reversal imaging algorithms applied to short-range UWB scattering data," *IEEE Int. Conf. Ultra-Wideband (ICUWB 2007)*, Singapore, Sep. 24–26, 2007.
8. Katko, A. R., S. Gu, J. P. Barrett, B.-I. Popa, G. Shvets, and S. A. Cummer, "Phase conjugation and negative refraction using nonlinear active metamaterials," *Phys. Rev. Lett.*, Vol. 105, No. 12, 123905–123905, 2010.
9. Belov, P. A. and Y. Hao, "Sub-wavelength imaging at optical frequencies using a transmission device formed by a periodic layered metal-dielectric structure operating in the canalization regime," *Phys. Rev. B*, Vol. 73, No. 11, 113110–113110, 2006.
10. Eleftheriades, G. and A. Wong, "Holography-inspired screens for sub-wavelength focusing in the near field," *IEEE Microw. Wireless Compon. Lett.*, Vol. 18, No. 4, 236–238, 2008.
11. Merlin, R., "Radiationless electromagnetic interference: evanescent-field lenses and perfect focusing," *Science*, Vol. 317, No. 5840, 927–929, 2007.
12. Malyuskin, O. and V. Fusco, "Far field subwavelength source resolution using phase conjugating lens assisted with evanescent-to-propagating spectrum conversion," *IEEE Trans. Antennas Propag.*, Vol. 58, No. 2, 459–468, 2010.
13. Memarian, M. and G. V. Eleftheriades, "Evanescent-to-propagating wave conversion in sub-wavelength metal-strip gratings," *IEEE Trans. Microw. Theory Tech.*, Vol. 60, No. 12, 3893–3907, 2012.
14. Ge, G.-D., B.-Z. Wang, D. Wang, D. Zhao, and S. Ding, "Subwavelength array of planar monopoles with complementary split rings based on far-field time reversal," *IEEE Trans. Antennas Propag.*, Vol. 59, No. 1, 4345–4350, 2011.
15. Katko, A. R., G. Shvets, and S. A. Cummer, "Phase conjugation metamaterials: Particle design and imaging experiments," *Journal of Optics*, Vol. 14, No. 11, 114003–114003, 2012.
16. Park, Y. K., "Subwavelength light focusing and imaging via wavefront shaping in complex media," *Progress In Electromagnetics Research Symposium Abstracts*, Guangzhou, China, August 25–28, 2014.
17. Sidorenko, P., Y. Shechtman, Y. C. Eldar, O. Cohen, and M. Segev, "Sparsity-based sub-wavelength imaging and super-resolution in time-resolved and spectroscopic instruments," *Progress In Electromagnetics Research Symposium Abstracts*, Guangzhou, China, August 25–28, 2014.
18. Mittra, R. (Ed.), *Computational Electromagnetics — Recent Advances and Engineering Applications*, Chapter 16, 553–574, Springer, New York, 2013.
19. Gu, X., C. Pelletti, R. Mittra, and Y. Zhang, "Resolution enhancement of phase-conjugating lenses by using signal processing algorithms," *IEEE Antennas Wireless Propag. Lett.*, Vol. 13, 511–514, 2014.

20. Gu, X., C. Pelletti, R. Mittra, and Y. Zhang, "Signal processing approach to electromagnetic sub-wavelength imaging," *IEEE Antennas and Propagation Society International Symposium (APS/URSI 2013)*, Orlando, Florida, July 7–13, 2013.
21. Gu, X., R. Mittra, and Y. Zhang, "Electromagnetic sub-wavelength imaging using the basis matrix method in conjunction with singular value decomposition (SVD) algorithm," *IEEE Antennas and Propagation Society International Symposium (APS/URSI 2014)*, Memphis, TN, July 6–11, 2014.
22. Mittra, R., X. Gu, and Y. Zhang, "Signal processing approach to realizing enhanced resolution from imaging systems such as lenses," *XXXIth URSI General Assembly and Scientific Symposium (URSI/GASS 2014)*, Beijing, China, August 17–23, 2014.
23. Balanis, C. A., *Modern Antenna Handbook*, Wiley, 2008.
24. Lafond, O., M. Himdi, H. Merlet, and P. Lebars, "An active reconfigurable antenna at 60 GHz based on plate inhomogeneous lens and feeders," *IEEE Trans. Antennas Propag.*, Vol. 61, No. 4, 1672–1678, 2013.
25. Luneburg, R. K., *Mathematical Theory of Optics*, University of California Press, 1964.
26. James, G., A. Parfitt, J. Kot, and P. Hall, "A case for the Luneburg lens as the antenna element for the square kilometre array radio telescope," *Radio Science Bulletin*, No. 293, 32–37, June 2000.
27. Hua, C., X. Wu, N. Yang, and W. Wu, "Air-filled parallel-plate cylindrical modified Luneberg lens antenna for multiple-beam scanning at millimeter-wave frequencies," *IEEE Trans. Microw. Theory Tech.*, Vol. 61, No. 1, 436–443, 2013.
28. Liang, M., X. Yu, S.-G., Rafael, W.-R. Ng, M. E. Gehm, and H. Xin, "Direction of arrival estimation using Luneburg lens," *IEEE International Microwave Symposium (IMS) Digest (MTT)*, 1–3, June 17–22 2012.
29. Jain, S. and R. Mittra, "Flat-base broadband multibeam Luneburg lens for wide angle scan," *IEEE Antennas and Propagation Society International Symposium (APS/URSI 2014)*, Memphis, TN, July 6–11, 2014.
30. Gu, X., S. Jain, R. Mittra, and Y. Zhang, "Enhancement of angular resolution of a flat-base Luneburg lens antenna by using correlation method," *Progress In Electromagnetics Research M*, Vol. 37, 203–211, 2014.
31. Mittra, R., C. Pelletti, N. L. Tsitsas, and G. Bianconi, "A new technique for efficient and accurate analysis of FSSs, EBGs and metamaterials," *Microw. Opt. Techn. Lett.*, Vol. 54, No. 4, 1108–1116, 2011.
32. Pelletti, C., G. Bianconi, R. Mittra, A. Monorchio, and K. Panayappan, "Numerically efficient method-of-moments formulation valid over a wide frequency band including very low frequencies," *IET Microw. Antennas Propag.*, Vol. 6, No. 1, 46–51, 2012.
33. FEKO Suite 6.2 [Online]. Available: www.feko.info.
34. Donoho, D. L., "Compressed sensing," *IEEE Trans. Inf. Theory*, Vol. 52, No. 4, 1289–1306, 2006.
35. Balanis, C. A., *Antenna Theory — Analysis and Design*, 2nd edition, John Wiley & Sons, 1982.
36. Mohimani, H., M. Babaie-Zadeh, and C. Jutten, "A fast approach for overcomplete sparse decomposition based on smoothed L0 norm," *IEEE Trans. Signal Process.*, Vol. 57, No. 1, 289–301, 2009.
37. Berg, E. V. D. and M. P. Friedlander, "Sparse optimization with least-squares constraints," *SIAM J. OPTIM.*, Vol. 21, No. 4, 1201–1229, 2011
38. Yu, W., X. Yang, Y. Liu, R. Mittra, and A. Muto, *Advanced FDTD Methods: Parallelization, Acceleration, and Engineering Applications*, Artech House, Norwood, MA, USA, March 2011.
39. Guru, B. and H. Hiziroglu, *Electromagnetic Field Theory Fundamentals*, 2nd edition, Cambridge University Press, 2004.